ELSEVIER

Ultramicroscopy 86 (2001) 191–206

ultramicroscopy

www.elsevier.nl/locate/ultramic

Fabrication of quantum well microcantilever photon detectors

P.G. Datskos[a,b,*], S. Rajic[a], L.R. Senesac[b], I. Datskou[c]

[a] *Oak Ridge National Laboratory, 1 Bear Creek Road, P.O. Box 2008, Oak Ridge, TN 37831-8039, USA*
[b] *University of Tennessee, 401 Nielsen Physics Building, Knoxville, TN 37996-1200, USA*
[c] *Environmental Engineering Group, Inc., 11020 Solway School Rd, Knoxville, TN 37931-2052, USA*

Received 31 May 2000

Abstract

We have developed a new method for fabricating quantum well microcantilever arrays that can be used in a variety of sensing applications. Microcantilevers with quantum wells allow real-time manipulation of energy states using external stress thus providing photon wavelength tunability. For example, this can result in an effective and rapid change in electron energy levels in photon detection devices. We applied this microfabrication technique to develop InSb microcantilevers and small arrays of GaAs/GaAlAs microcantilever quantum wells. Such arrays can be useful in the detection of infrared (IR) radiation at room temperature. © 2001 Elsevier Science B.V. All rights reserved.

Keywords: Quantum well; Photon detectors

1. Introduction

Photonics is important to a large number of applications both commercial and military. In particular, detection and imaging of infrared (IR) radiation has extensive medical, industrial, military, and commercial applications. IR radiation is loosely defined as photons with wavelengths from 0.7 to 50 μm. IR radiation is the second most intense radiation source in our environment and can pass through many crystalline, plastic and gaseous materials including the earth's atmosphere. Most IR detectors take advantage of two atmospheric transmission "windows": the 3–5 μm window and the 8–14 μm window (see Fig. 1(a)). Most of the IR radiation emitted from objects at room temperature is in the 8–14 μm region (see Fig. 1(b)). IR detection applications range from thermal imaging, astronomy, biomedical diagnostics, and IR spectroscopy to name a few. A limiting factor to imaging in the IR spectrum has been the high cost of IR cameras. Infrared radiation detectors [1–4] can be classified broadly as either quantum (electro-optic/photon) detectors [5] or thermal detectors such as pyroelectric [6], thermoelectric, resistive microbolometers [7–10], and micromechanical thermal detectors [11–18].

Electro-optic detectors are based on the conversion of electromagnetic energy to electronic excitation in semiconductor crystals. Traditionally, such electronic excitation is detected as a change in the electrical conductivity of the material. Electro-optic IR detectors exhibit fast response times and high detectivities,

*Corresponding author. Tel.: +1-865-574-6205; fax: +1-865-574-9704.
E-mail address: pgd@ornl.gov (P.G. Datskos).

0304-3991/01/$ - see front matter © 2001 Elsevier Science B.V. All rights reserved.
PII: S0304-3991(00)00072-3

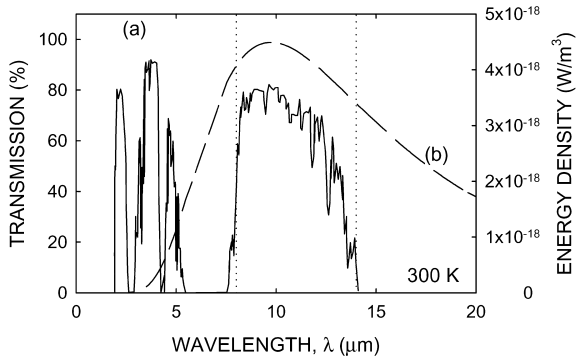

Fig. 1. Atmospheric transmission windows for IR radiation: (a) Transmission as a function of photon wavelength. Most IR detectors take advantage of the windows of transmission from 3 to 5 μm and from 8 to 14 μm. (b) blackbody radiation as a function of photon wavelength for an object at 300 K. Most of the IR radiation emitted is in the 8–14 μm window (wavelength region between the two vertical dotted lines.).

D^*, but require the devices to be kept at a reduced temperature to minimize the effects of internal thermal noise that varies as $\exp(-\varepsilon_g/kT)$; ε_g is the band-gap energy, k is Boltzmann's constant and T is the temperature. On the other hand, thermal detectors have a very broadband response, since they are based upon thermal conversion of the absorbed energy. The thermoresistive microbolometer [9,10,19,20] detector and electric field enhanced pyroelectric detectors [6,21] have demonstrated a noise equivalent temperature difference (NETD) of less than 50 mK. For a 320×340 array with $50\,\mu m \times 50\,\mu m$ pixel size an NETD of <20 mK was demonstrated [19]. Recently, a new type of thermal detector based on micromechanical structures was developed [14,16–18,22,23] with a reported NEDT ranging from 5 K [17] to 5 mK [16,23] and $D^* \sim 10^8\,cm\,Hz^{1/2}\,W^{-1}$ [14]. However, these thermal detectors generally have slow response times ($>$ms), low detectivities, and are limited by the fundamental temperature coefficient of resistance (for resistive bolometers), the pyroelectric coefficient (for pyroelectric detectors) and thermal bending sensitivity (for micromechanical systems). Hence fundamentally new detection techniques are required for the development of compact, light-weight, broadband, highly-sensitive, and low-power consumption IR imaging sensors.

More recently we have developed a new approach for producing compact, light-weight, highly sensitive micromechanical photon detectors that are based on micro-electro-mechanical systems (MEMS). These new types of semiconductor micromechanical detectors operate as photon detectors based on the photo-induced stress in semiconductors [24–27]. The operation relies on the interaction of photons directly with the semiconductor material, semiconductor/metal interface, or microcantilever quantum wells resulting in photo-induced stress. The photo-induced stress is then detected as a change in the radius of curvature of the micromechanical system. Earlier work has shown that microcantilever bending can readily be determined by a number of means, including optical, piezoresistive, capacitive, and electron tunneling with extremely high sensitivity [28,29]. For example, the metal-coated microcantilevers that are commonly employed in atomic force microscopy (AFM) allow sub-Angstrom ($<10^{-10}$ m) sensitivity to be routinely obtained.

In the present work we discuss a new microfabrication process for both thermal and photonic microstructures with quantum wells. When micromechanical structures are used as photon detectors and not as thermal detectors, they have faster response times and higher performance than that of microcantilever thermal detectors. Since the transduction mechanism relies on mechanical stress we first discuss the thermally induced and photo-induced stress in semiconductor and quantum well microcantilevers. We then address the issue of the fundamental noise sources in these systems and finally we discuss our microfabrication approach.

2. Thermally induced stress

Bimaterial microcantilevers undergo bending due to differential stress in the microcantilever. The change in the radius of curvature, R, due to differential stress, Δs, can be written as [14,30]

$$\frac{1}{R} = \frac{6(1+(t_1/t_2)^2)}{l(t_1+t_2)[3(1+t_1/t_2)^2+(1+t_1E_1/t_2E_2)(t_1^2/t_2^2+t_2E_2/t_1E_1)]}\frac{\Delta s}{E^*}, \tag{1}$$

where t_1 and t_2 are the thickness of the coating and microcantilever substrate, l is the microcantilever length, E_1 and E_2 are the Young's moduli of the coating and microcantilever, and E^* is the effective Young's modulus of the coated microcantilever. Note that $E^* = E_1E_2/(E_1+E_2)$. Bending resulting from differential stress in such a microstructure can be detected with sub-nanometer sensitivities. The bending $z_{\max}$ is related to the radius of curvature R by $z_{\max} = l^2/(2R)$ which can be rewritten as

$$z_{\max} = \frac{3l}{t_1+t_2}\left[\frac{1+(t_1/t_2)^2}{3(1+t_1/t_2)^2+(1+E_1/t_2E_2)(t_1^2/t_2^2+t_2E_2/t_1E_1)}\right]\frac{\Delta s}{E^*}. \tag{2}$$

Previous work has shown that silicon nitride microcantilevers with a thin gold film on one side undergo measurable bending due to temperature changes as small as 10^{-6} K. This bending is due to the differential stress created by dissimilar thermal expansion of the microcantilever substrate and the gold coating (or the bimaterial effect). The differential stress due to thermal expansion of these materials can be approximated as [14]

$$\Delta s \approx (E_1\alpha_1 - E_2\alpha_2)l\Delta T, \tag{3}$$

where ΔT is the temperature change and α_1 and α_2 are the coefficients of thermal expansion for the materials composing the bimaterial strip. By measuring the bending distance $z_{\max}$, the change in temperature can be determined by

$$z_{\max} = \frac{3l^2}{t_1+t_2}\left[\frac{1+(t_1/t_2)^2}{3(1+t_1/t_2)^2+(1+t_1E_1/t_2E_2)(t_1^2/t_2^2+t_2E_2/t_1E_1)}\right]\frac{E_1\alpha_1 - E_2\alpha_2}{E^*}\Delta T. \tag{4}$$

This assumes the ideal case where the microcantilever and its base are at the same temperature. We have also assumed that all incident radiation is absorbed by the microcantilever and the base, resulting in a uniform temperature change. The fundamental limits to the performance of these micromechanical structures are established by the properties of the microcantilevers themselves and also depend on the readout means. When an optical readout scheme is used in certain cases, the influence of the optical readout can be negligible. The fundamental limits i.e., background fluctuation noise limit and temperature fluctuation noise limit depend on the inherent properties of the microcantilever (see later section). An ideal, noiseless readout would amplify and display the signal and noise inherent to the microstructures without adding any excess noise. It turns out that the optical readout investigated in this work is very close to this ideal case [31,32].

3. Photo-induced electronic stress

Microcantilevers exposed to photons undergo bending due to the differential surface stress [24,33] ($\Delta s = s_1 - s_2$) created by transient expansions; the top (photon exposed) side expands sooner than the bottom (unexposed) side thus creating a differential surface stress. When the structure is bimaterial (see

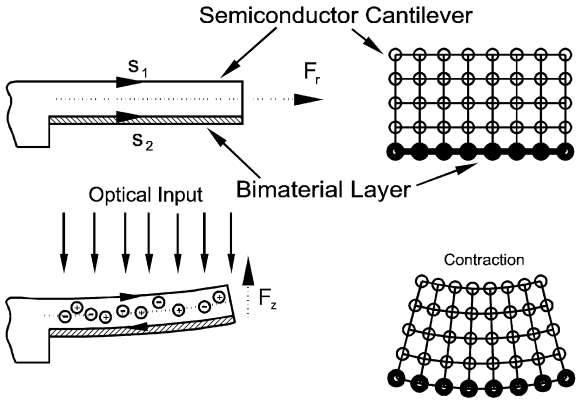

Fig. 2. Schematic diagram showing the bending process of a semiconductor microcantilever exposed to photons. Surface stresses s_1 and s_2 are balanced at equilibrium. Also depicted is the accompanied contraction of the silicon lattice following the generation of electron–hole pairs.

Fig. 2) the bending is primarily due to the differentiated response of the two materials. Earlier work has shown that the absorption of photons by a solid results in temperature changes and thermal expansion which in turn gives rise to acoustic waves at frequencies corresponding to the amplitude modulation of the incident photon beam [34,35]. It is well known that in a semiconductor the generation of "free" charge carriers (electrons and holes) via photon irradiation results in the development of a local mechanical strain [36,37]. This additional strain adds to other strains resulting from temperature changes of the semiconductor. When the photon flux is high enough to cause the semiconductor to heat, the subsequent expansion (or contraction) can be detected as acoustic waves with conventional photoacoustic techniques [35,38].

In a semiconductor structure of thickness t and energy bandgap ε_g, the change in total surface stress due to photogenerated change in the charge carrier density, Δn will be given by [24,36,37,39]

$$\Delta s = \Delta s_{\mathrm{pi}} = \left(\frac{1}{3}\frac{\mathrm{d}\varepsilon_g}{\mathrm{d}P}\Delta n\right)E, \tag{5}$$

where, $\mathrm{d}\varepsilon_g/\mathrm{d}P$ is the pressure dependence of the energy bandgap, and E is the Young's modulus of the semiconductor structure. When $\mathrm{d}\varepsilon_g/\mathrm{d}P$ is negative the photo-induced stress is of opposite sign than that of the thermal stress and will tend to make the semiconductor crystal contract. The deflection sensitivity can be enhanced by coating the microcantilever with a layer of another material. For a rectangular bimaterial bar (Fig. 2) of length l, width w, and total thickness t, the reciprocal of the radius of curvature is given again by

$$\frac{1}{R} = \frac{2(1+(t_1/t_2)^2)}{(t_1+t_2)[3(1+t_1/t_2)^2+(1+t_1E_1/t_2E_2)(t_1^2/t_2^2+t_2E_2/t_1E_1)]}\left(\frac{\mathrm{d}\varepsilon_g}{\mathrm{d}P}\Delta n\right)\frac{E_1}{E^*}. \tag{6}$$

Materials with large differences in E will offer better deflection sensitivity. However, the larger the difference between the Young's moduli the more difficult it becomes to deposit a bimaterial layer and not produce "curled" microcantilevers [16,40]. The deposition of metal layers on thin microcantilevers to produce unstressed structures with no bending is difficult and requires extremely high thermal stability. Bimaterial microcantilevers with no noticeable bending have been produced when care was taken to avoid any temperature rises during the bimaterial deposition process [40]. In those studies the investigators broke

down the complete deposition process into 20 steps in order to avoid the temperature of the microcantilever rising during the deposition.

The reciprocal of the radius of curvature is approximately equal to d^2z/dy^2 [41]. Then, using Eq. (6) the maximum displacement z_{max} of the microcantilever is given by

$$z_{max} = \frac{l^2}{t_1 + t_2}\left(\frac{1 + (t_1/t_2)^2}{3(1 + t_1/t_2)^2 + (1 + t_1E_1/t_2E_2)(t_1^2/t_2^2 + t_2E_2/t_1E_1)}\right)\frac{E_1}{E^*}\frac{d\varepsilon_g}{dP}\Delta n. \tag{7}$$

The overall change in z_{max} will depend on several physical and mechanical properties of the semiconductor. In fact, for the same input power a Si microcantilever exhibits a photo-induced bending that is about four times larger than that due to thermal induced stress [24].

Assuming that an incident radiant power, Φ_e, in asemiconductor microcantilever generates a number density of excess charge carriers, Δn, we get

$$\Delta n = \eta\frac{\lambda}{hc}\frac{\tau_L}{lw(t_1 + t_2)}\Phi_e, \tag{8}$$

where η is the quantum efficiency, $h(= 6.626 \times 10^{-34}\,\mathrm{J\,s})$ is Planck's constant, $c(= 3 \times 10^8\,\mathrm{m\,s^{-1}})$ is the speed of light, and τ_L is the lifetime of the carriers in the semiconductor. Then the maximum displacement z_{max} can be rewritten as

$$z_{max} = \frac{l}{w(t_1 + t_2)^2}\left(\frac{1 + (t_1/t_2)^2}{3(1 + t_1/t_2)^2 + (1 + t_1E_1/t_2E_2)(t_1^2/t_2^2 + t_2E_2/t_1E_1)}\right)\frac{E_1}{E^*}\eta\frac{\lambda}{hc}\frac{d\varepsilon_g}{dP}\tau_L\Phi_e. \tag{9}$$

We can define the deflection responsivity $\Re = z/\Phi_e$, viz.,

$$\Re = \frac{l}{w(t_1 + t_2)^2}\left(\frac{1 + (t_1/t_2)^2}{3(1 + t_1/t_2)^2 + (1 + t_1E_1/t_2E_2)(t_1^2/t_2^2 + t_2E_2/t_1E_1)}\right)\frac{E_1}{E^*}\eta\frac{\lambda}{hc}\frac{d\varepsilon_g}{dP}\tau_L. \tag{10}$$

Since the charge carriers can be generated in a very short time, the photo-induced stress can manifest itself much faster than thermal stress.

In Fig. 3 we calculated the photo-induced responsivity as a function of photon wavelength for a number of different semiconductor materials using Eq. (10) and the material properties found in Table 1 [4,42,43]. In these calculations we assumed the microcantilevers had length $l = 100\,\mu\mathrm{m}$, width $w = 20\,\mu\mathrm{m}$, and total thickness $t = 0.5\,\mu\mathrm{m}$. The bending due to photo-generated charges increases linearly with increasing wavelength up to the cutoff λ_c.

4. Microfabrication method

4.1. Microfabrication process flow

The process for the fabrication of these novel microcantilevers includes the following major steps: (i) substrate preparation, (ii) molecular beam epitaxy of the quantum wells, (iii) single-point diamond turning, (iv) broad ion beam thinning, (v) focused ion beam patterning, and (vi) pulsed laser deposition metalization. The traditional silicon-based microelectronic integrated circuit fabrication processes typically involve substantial wet and dry chemistry to create microstructures of interest. However, such processes are not well understood for many alternate semiconductor materials and therefore it is rather difficult to apply these processes to the fabrication of microcantilevers. Furthermore, microstructures often collapse due to liquid surface tension effects at the release stage. Even when dry processing, such as reactive ion etching, is

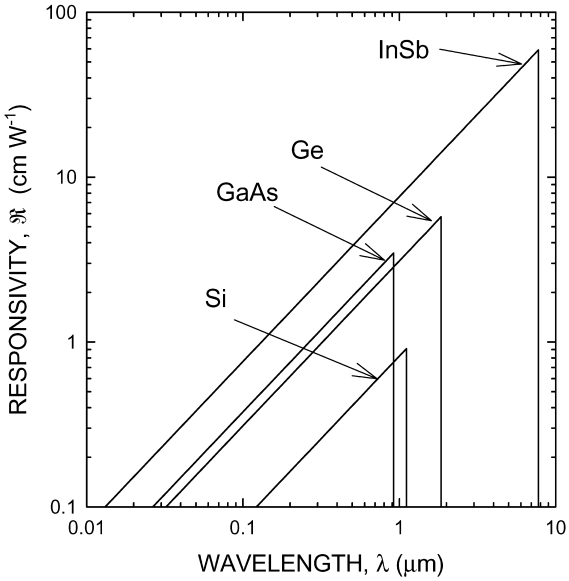

Fig. 3. Calculated responsivity, ℜ, for semiconductor microcantilevers as a function of photon wavelength, for different materials.

Table 1
Properties of semiconductor materials that can be used as microcantilever photon detectors

Semiconductor material	ε_g (eV)	$d\varepsilon_g/dP$ (10^{-24} cm^3)	E (GPa)	G (W m^{-1} K^{-1})
GaAs	1.35[a]	−13.67[b]	85.5	55
Si	1.12[a]	−3.14[c]	130.91	163
Ge	0.67[a]	11.52[c]	102.66	59
InSb	0.16[a]	23.61[c]	42.79	36

[a] From Ref. [4].
[b] From Ref. [48].
[c] From Ref. [43].

extensively employed the fabrication will be highly material dependent. Therefore, assuming it is chemically possible, new process parameters will be required for every material system. As a result we have chosen an essentially material independent and dry novel fabrication and hybridization approach. In the fabrication of microcantilevers there are basically two options, precision material deposition and/or removal. We have employed a number of tools for both approaches that have been used in novel ways to directly fabricate microdevices from material substrates of interest. The rapid device prototyping technique shown in Fig. 4 is amenable to most group III–V and II–VI semiconductors.

4.2. Molecular beam epitaxy

The epitaxial process chosen for this quantum well work was molecular beam epitaxy (MBE) since we required considerable heterostructure interface control. This technique has long been known to produce high-quality material with ~0.3 nm compositional control at the expense of growth speed (~ monolayer per

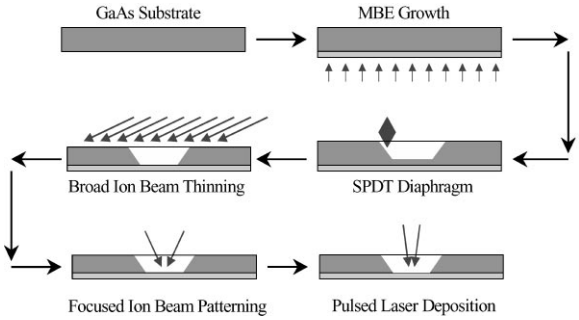

Fig. 4. Process flow for the advanced microfabrication technique used for rapid device prototyping.

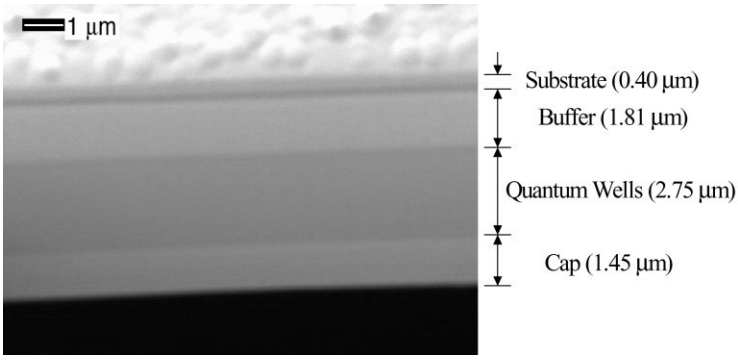

Fig. 5. Cross-sectional image of MBE grown quantum well layers.

Table 2
Parameters of the quantum well material used in the present study

Layer[a]	Material	Thickness (nm)	First repeat	Second repeat
Quantum well	GaAs	6.0	—	× 40
Quantum barrier	$GaAl_xAs_{1-x}$[b]	4.3	× 10	
Quantum well	GaAs	1.1		
Quantum barrier	$GaAl_xAs_{1-x}$[b]	4.3	—	

[a] Made available from Sanders a Lockheed Martin company, with absorption wavelength at 8.6 μm.
[b] $x = 0.3$.

second). However this shortcoming is acceptable due to the very large substrate growth areas and monolayer compositional control that are possible with MBE. Commercial 75 mm diameter GaAs substrate surfaces are of insufficient quality for precise heterostructure interface control, and therefore the following process was chosen for our project. First an n-doped GaAs buffer layer with a thickness of 1.8 μm was grown with MBE. This was followed by the growth of approximately 400 wells and barriers to a total thickness of ~2.75 μm (see Fig. 5). Finally, a GaAs cap layer with a thickness of 1.45 μm was grown. In further processing the substrate and both the buffer and cap layers are completely removed to form the fully released microcantilevers which are only ~1 μm thick. The details of the quantum well structures are shown in Table 2. The basic GaAlAs/GaAs barrier/well cell is repeated 10 times. Each of these cells is encapsulated between a GaAs/GaAlAs well/barrier. This super cell is then repeated 40 times to form the entire multiple

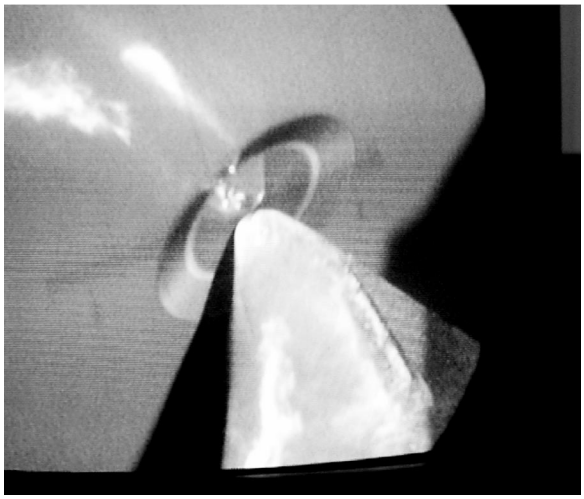

Fig. 6. Example of a 2 mm diameter, $<10\,\mu m$ thickness conical semiconductor depression (diaphragm) during single-point diamond turning.

quantum well (MQW) region. In all cases the Al content was 30%. This MQW layer produced an equivalent energy band structure for a wide photon absorption region which peaked at 8.6 μm.

4.3. Single point diamond turning (SPDT)

Since the goal in our fabrication scheme was to maximize material independence of the process, it was important in the material removal mode of this approach to remove the maximum amount of material before proceeding to the next more material-dependent fabrication step, if required. Unlike conventional etching processes, precision direct write techniques can be used to rapidly and precisely remove material without many of the problems associated with traditional photolithography-based etching processes used to create silicon features. Even though there is some inherent material dependence associated with almost every process, these effects were negated since almost 99% of the material removal was accomplished with precision SPDT. This created a diaphragm, as can be seen in Fig. 6, that is amenable to further direct write fabrication techniques. Furthermore, eliminating or substantially reducing dependence on etchants will substantially decrease the time consuming step of matching a specific etching agent to the target binary, ternary, or quaternary material.

Using our diamond turning facility we were able to explore many "exotic" semiconductor material systems. Two diamond turning machines were available for this project: (i) the prototype of the Nanoform 600 class machine, that can diamond turn parts with diameters of 0.6 m with a positioning resolution of 1.25 nm; and (ii) the Precitech Optimum 2800 that was particularly amenable to semiconductor micromachining.

The micromachining conditions used for all materials in the final surface passes were: rotational speed of 2000 rpm; feed rate of 500 μm/min.; cut depth of 0.5 μm; and diamond tool radius of 0.508 mm. However, the roughing cut parameters varied according to the individual material properties. The quality of the micromachined surfaces was critical since these thin diaphragm surfaces serve as the substrates for the eventual microdevices. All of the non-silicon starting substrate wafers were polished on the vacuum fixture side and lapped on the diamond tool side. Thus the final microdevices have a polished side and a diamond turned/ion milled side. An atomic force microscope image of a silicon micromachined surface is depicted in

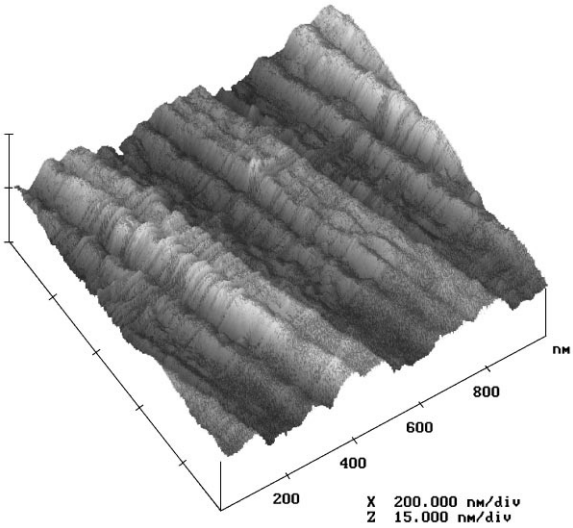

Fig. 7. AFM image after SPDT of semiconductor surface [(1 0 0) silicon]. Most alternate materials (II–VI and III–V) show superior results compared to this hard/brittle material.

Fig. 7. Although at first glance this silicon surface appears highly textured, the scale indicates the extreme exaggeration of the vertical (z-axis) dimension in this image. The peak to valley deviation is approximately 5 nm. Two distinct periods can be seen. The larger period of approximately 300 μm corresponds to the expected values given the feed rate, rotational speed, and depth-of-cut. However, the other pattern has a higher frequency component induced by vibration. Fortunately, most of the important group II–VI and III–V semiconductors are even more amenable, to varying degrees, than silicon to this fabrication process. InSb- and GaAs-based material systems were of particular interest in this study.

4.4. Ion beam milling

In our studies we extensively employed both broad and focused ion beam material removal techniques. The SPDT process produced well-controlled ~10 μm thick semiconductor diaphragms. However, mechanical micromachining material removal processes introduce subsurface damage on the order of the depth of cut. Thus under the machining conditions used in the SPDT final cut, a maximum ~5 μm of subsurface damage would be produced. This damage can be removed, and the semiconductor diaphragm further thinned, with broad ion beam milling. However, compound single crystal semiconductors typically roughen under ion beam bombardment due to preferential sputtering one constituent in the crystal compared to the others. We have developed a technique to mitigate this effect and even provide smoothing in many cases. The substrate was rotated and the ion beam impinged at angles as high as 70° from the surface normal. The process conditions involved a 3 cm argon ion beam at 500 V and 20 mA. This technique both removed the SPDT induced subsurface damage and thinned the diaphragm to the required thickness for focused ion beam patterning. All crystalline compound semiconductors are susceptible to ion beam roughening to different degrees, with InSb showing the most severe damage compared to moderate roughening produced in GaAs/GaAlAs.

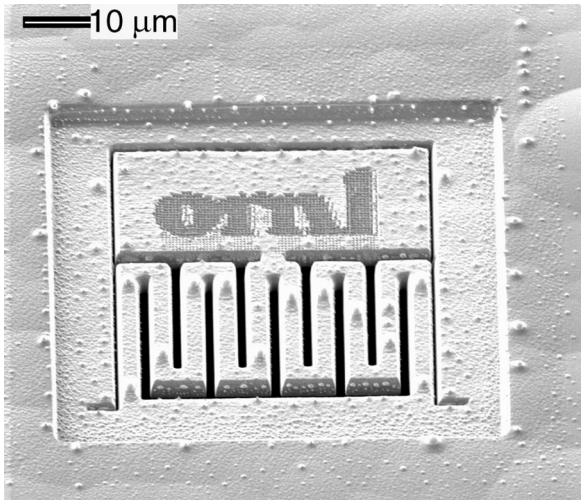

Fig. 8. FIB patterning of individual micromechanical quantum well detector element.

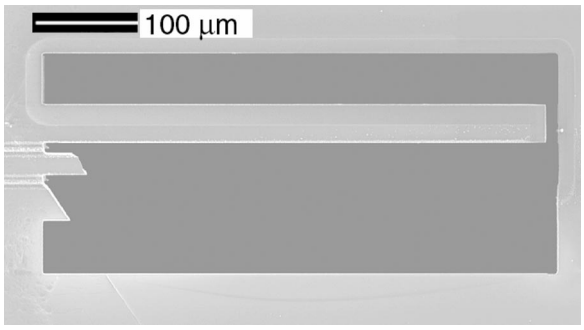

Fig. 9. FIB milling of InSb diaphragm that produces an InSb microcantilever device used for subsequent IR response studies.

4.5. Focused ion beam milling

We also used in our studies a focused ion beam (FIB) milling system (FEI 200) to pattern our devices. The FIB system uses a Ga ion source to produce an energetic ion beam focused onto the working surface [44–46]. The beam energy was 30 keV and the beam current varied (1 pA to 11.5 nA), depending on the focused beam diameter (25–600 nm). The system utilizes secondary electron emission produced by the scanning ion beam to image the surface in a manner similar to an electron microscope. This allows the region of the surface being modified to be observed before and during the ion milling process. Magnifications achievable are similar to electron microscopes, ranging from 190 to over 100,000. This FIB system was used to direct write a pattern, such as the ones shown in Figs. 8 and 9, by rastering the ion beam over a user-defined area on the thinned semiconductor surface.

5. Experimental

In the present work we studied microcantilever structures that were made from single crystal InSb and GaAs/GaAlAs quantum wells using the process described earlier. In Fig. 9 we show an example of an InSb

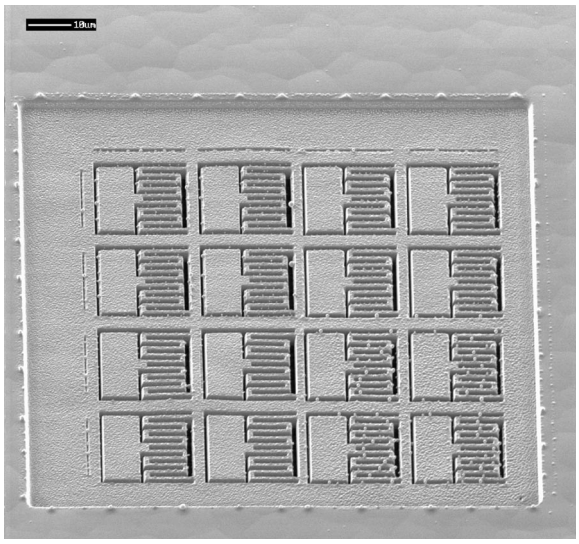

Fig. 10. Micromachined arrays of micromechanical quantum well devices.

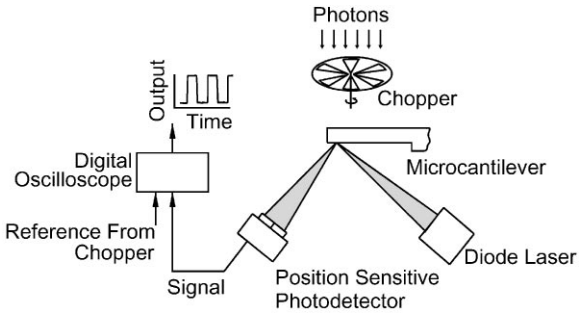

Fig. 11. Schematic of the experimental setup and the optical readout scheme used in the present studies.

microcantilever and in Fig. 10 we show a small 4×4 array of microstructures made from GaAs and GaAlAs quantum wells Although bending of such microcantilevers can readily be determined by a number of means (optical, capacitive, electron tunneling, and piezoresistive methods), in this work we concentrated on optical readout techniques. It turns out that the optical readout technique adds negligible noise in the detector system [31,32]. The optical readout approach used in the present studies was adapted from atomic force microscopy imaging systems [47] and is shown in Fig. 11. Microcantilevers were mounted in a chip holder which, in turn, was mounted on a three-axis translation stage to facilitate fine adjustment of the microcantilever relative to the rest of the experimental apparatus. A mechanical chopper was used to modulate the incoming photon radiation.

A diode laser was used in a probe configuration to monitor bending. A laser beam was focused onto the tip of the microcantilever using a $10 \times$ microscope objective; in order to minimize heating of the tip by the probe laser, optical power was reduced by using a neutral density filter. A quad-element (A,B,C,D) photodiode detector was used to collect the reflected probe beam. The current output ($i_{A,B,C,D}$) of the photodiode depends linearly on the bending of the microcantilever. A high narrow bandpass optical filter is

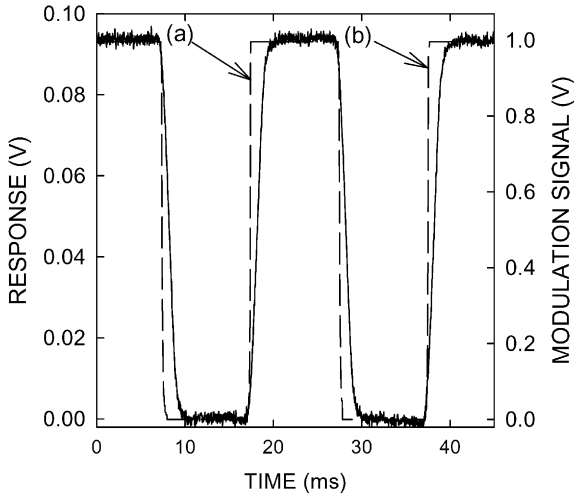

Fig. 12. Deflection [curve (a)] of a InSb microcantilever due to photo-induced stress when exposed to photons from a blackbody source. The dashed curve (b) represents the signal from the modulator and shows the amount of time the microcantilever was exposed to photons.

placed in front of the photodiode allowing the laser beam to be detected while preventing other wavelengths from reaching the photodiode. The amplified differential current signal from the quad cell photodiode, $i_{A,B,C,D}[= (i_A + i_B) - (i_C + i_D)/ (i_A + i_B + i_C + i_D)]$, is monitored and recorded using a digital oscilloscope or sent to a lock-in amplifier for signal extraction and averaging. This configuration provided a flexible, easily controlled test system for quantifying microcantilever response to optical energy. All measurements were conducted at ambient temperature and atmospheric conditions.

6. Results and discussion

We used the fabrication method described earlier in Section 4 to develop InSb microcantilevers and GaAs/GaAlAs quantum well microstructures. The InSb microcantilever shown in Fig. 9 was a 500 μm long micromechanical structure and was patterned in the middle of a 6 μm thick InSb diaphragm using FIB. The missing material simply dropped out once the pattern was complete, leaving released microcantilevers. The deflection response of this microdevice due to exposure to energy from a 500°C blackbody source is shown in Fig. 12. A Si window was used to allow only photons with wavelengths $\lambda > 1.1$ μm. The experimental setup used for these measurements was discussed in the previous section. We found that the single crystal InSb microcantilever IR detector used exhibited enhanced deflection response (both magnitude and frequency) due to photo-induced compared to simple thermomechanical (bimaterial) movement due to thermal stress in the lattice [24]. The measured response shown in Fig. 12 corresponds to a bending of 55 nm when the measured signal was 93 mV which corresponds to a sensitivity of 0.59 nm/mV.

The micromechanical quantum well devices shown in Fig. 10 were designed to be used as elements of a larger IR imaging array. The geometry was chosen to represent a square "pixel" in such an imaging array. Using quantum well structures to detect photons possess a number of advantages. As can be seen from Table 1 the choice of materials for photon detection depends on the cut-off wavelength which is fixed for single or binary materials. However, the band-gap energy can be engineered using quantum well devices for a specific wavelength or a band of wavelengths. Furthermore, when quantum wells are part of a

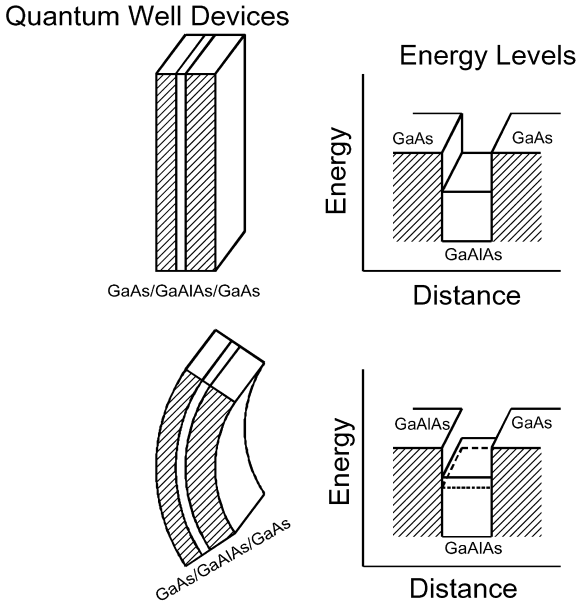

Fig. 13. Modulation of energy levels in a micromechanical quantum well device using external stress.

microstructure the band-gap energy can also be tuned by stressing the microstructure (see Fig. 13 and later in this section); expanding the quantum well leads to a lowering of the energy level in the well.

The GaAs/GaAlAs quantum well microcantilever shown in Fig. 8 was a $50\,\mu m \times 50\,\mu m$ pixel with a thickness of about $3.5\,\mu m$. Cantilevers were fabricated in the middle of a GaAs/GaAlAs quantum well diaphragm using the FIB techniques described above. We measured the deflection response of this microdevice when exposed to photons from an IR source; the IR source was a calibrated blackbody and its temperature was set at 900°C. In Fig. 14 we plot the bending response to modulated incoming photons as a function of time. In this experiment, photons from the IR source passed through a 10 mm in diameter circular aperture and a mechanical chopper was used to modulate the IR photons; the width of the opening in the blades of the chopper wheel was about twice the aperture diameter of the IR source. Since light from the entire aperture illuminates the microcantilever device, it takes about one quarter of the period of the chopper to fully expose or block the energy from the IR source. This affects the apparent time constant of the device as can be seen in Fig. 14. We found that it takes about one-fourth of the modulation period for the microcantilever to reach its maximum response, and then another quarter period for the response to relax back to zero. The actual time response of the IR microcantilever is much faster than shown in this observation, and at a maximum modulation speed of about 450 Hz, the shape of the response appeared unchanged. The motion of the device was calibrated by rotating the device in a precision rotation stage (part of the experimental set-up) and measuring the change in output voltage from the detector as a function of rotation angle. Since the deflection of the cantilever is a function of this rotation angle, a deflection calibration of 0.25 nm/mV was obtained. The response shown in Fig. 14 corresponds to a device deflection of about 15 nm.

We also investigated the tunability of micromechanical quantum wells using mechanical stress. The energy levels in the quantum wells are sensitive to applied external mechanical stresses. There are a number of ways one can study the effect of external mechanical stresses. For example, if a thin layer of magnetic material is deposited on the microcantilever surface, an applied external magnetic field will cause the

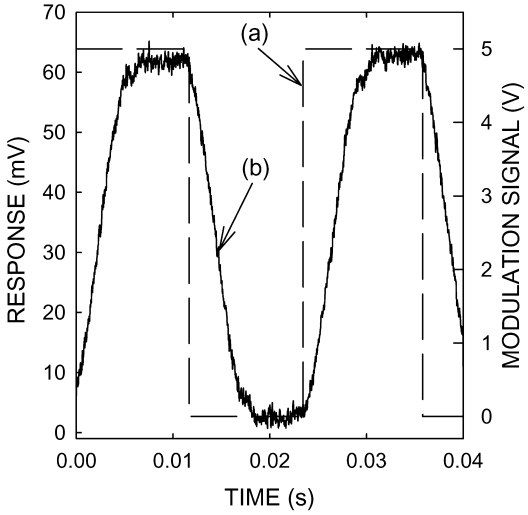

Fig. 14. Deflection of a GaAs/GaAlAs quantum well microstructure when exposed to photons from a blackbody source. The dashed curve (a) represents the signal from the modulator and shows the amount of time the microcantilever was exposed to photons. The linear appearance of the rise and fall portions of the response (b) is due to the opening and closing of the mechanical chopper and is therefore not representative of the device response time.

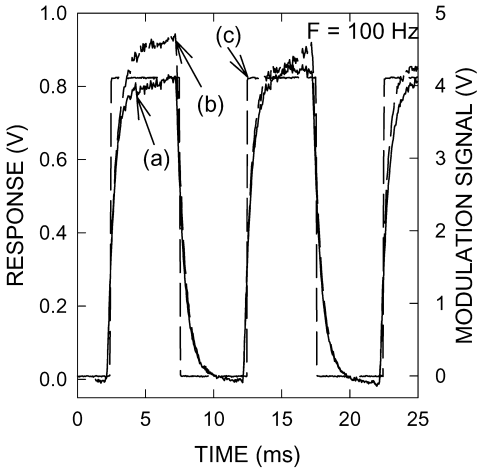

Fig. 15. Temporal response of micromechanical quantum wells to IR radiation. Curve (a) shows the response of the microcantilever when no external stress is applied and curve (b) represents the response when acoustic excitation of the microstructure is present. The photons from the IR source were modulated at 100 Hz [curve (c)].

microcantilever to bend. We used a somewhat simpler approach by exposing the microcantilever to an acoustic excitation source with frequencies over two orders of magnitude higher that the modulation frequency of the IR source. In Fig. 15 we plotted the response of the micromechanical quantum wells to IR radiation. In curve (a) we show the response when no external stress is applied while in curve (b) we plotted the response when the quantum well microstructure is acoustically excited. Photons from the IR source were modulated at 100 Hz [curve (c)]. We attributed the observed increase in the measured signal when

acoustic excitation is present to the broadening of the quantum well energy levels which occurs as a consequence of the applied mechanical stress. Although more studies of this effect are underway, our present results represent the first attempts to study energy level shifts in suspended two-dimensional electron gas (2DEG) systems.

7. Conclusions

We developed a microfabrication technique that can be applied to almost any material system. We used this technique to develop micromechanical quantum detectors made from InSb microcantilevers and GaAs/GaAlAs quantum well microstructures. Although SPDT and FIB are traditionally used for other purposes, these processes can readily be applied to the fabrication of microcantilevers from single-crystal materials and quantum wells. In our present studies semiconductor wafers with starting thicknesses of approximately 0.5 mm were rapidly thinned to less than 10 μm, producing diaphragms over a central region of the wafers approximately 2 mm in diameter. These diaphragms were subsequently ion-milled using a broad ion beam and a focused ion beam to produce within the diaphragm fully released microstructures and small arrays of microstructures. The microfabrication techniques employed were aimed to demonstrate micromechanical IR devices made from InSb and GaAs quantum wells. Microdevices that can be fabricated from silicon will always enjoy a substantial cost advantage over the techniques discussed above. However, for applications where particular silicon material parameters are not suitable, the present device prototype microfabrication approach is essentially a straightforward and relatively low-cost alternative.

Acknowledgements

We would like to thank Drs. Mani Sundaram and Thomas S. Faska of Sanders, a Lockheed Martin company, for providing the grown MBE wafers. We are grateful to Dr. T. Thundat for the AFM image of Fig. 7. The work performed by Oak Ridge National Laboratory was supported by DARPA, and the Laboratory Director's Research and Development Program of Oak Ridge National Laboratory. Oak Ridge National Laboratory is operated for the US Department of Energy by UT-Battelle, LLC, under contract DE-AC05-00OR22725. The work performed by the University of Tennessee was supported by the NSF Grant ECS-9727208. The work performed by EEG, Inc. was supported by the US Air Force contract F33615-99-C1431.

References

[1] J.L. Miller, Principles of Infrared Technology, Van Nostram Reinhold, New York, 1994.
[2] R.J. Kayes, Optical and Infrared Detectors, Vol. 19, Springer, Berlin, 1977.
[3] E.L. Dereniak, D.G. Crowe, Optical Radiation Detectors, Wiley, New York, 1984.
[4] E.L. Dereniak, G.D. Boreman, Infrared Detectors and Systems, Wiley, New York, 1996.
[5] A. Rogalski, Infrared Phys. Technol. 35 (1994) 1.
[6] C. Hanson, Infrared Technol. XXI SPIE-020 (1993) 330.
[7] R.A. Wood, Infrared Technol. XXI SPIE-2020 (1993) 322.
[8] R.A. Wood, N.A. Foss, Laser Focus World (1993) 101.
[9] P.W. Kruse, Infrared Technol. XXI SPIE-2552 (1995) 556.
[10] N. Butler, R. Blackwell, R. Murphy, R. Silva, C. Marshall, Infrared Technol. XXI SPIE-2552 (1995) 583.
[11] P.G. Datskos, P.I. Oden, T. Thundat, E.A. Wachter, R.J. Warmack, S.R. Hunter, Appl. Phys. Lett. 69 (1996) 2986.
[12] P.I. Oden, E.A. Wachter, P.G. Datskos, T. Thundat, R.J. Warmack, Infrared Technol. XXII SPIE-2744 (1996) 345.
[13] P.I. Oden, P.G. Datskos, T. Thundat, R.J. Warmack, Appl. Phys. Lett. 69 (1996) 3277.

[14] E.A. Wachter, T. Thundat, P.G. Datskos, P.I. Oden, S.L. Sharp, R.J. Warmack, Rev. Sci. Instr. 67 (1996) 3434.
[15] S. Rajic, B.M. Evans, P.G. Datskos, P.I. Oden, G. Thundat, C.M. Egert, Infrared Spaceborne Remote Sensing IV SPIE-2817 (1996) 179.
[16] R. Amantea, C.M. Knoedler, F.P. Pantuso, V.K. Patel, D.J. Sauer, J.R. Tower, in An Uncooled IR Imager with 5 mK NEDT, Orlando, FL, 1997, p. 210.
[17] M. Mao, T. Perazzo, O. Kwon, Y. Zhao, A. Majumdar, J. Varesi, P. Norton, in Infrared Vision Using an Uncooled Thermo-opto-mechanical Camera; Design, Microfabrication, and Performance, Nashville, TN, 1999, The American Society of Mechanical Engineers, New York, 1999, p. 309.
[18] T. Perazzo, M. Mao, O. Kwon, A. Majumdar, J.B. Varesi, P. Norton, Appl. Phys. Lett. 74 (1999) 3567.
[19] W. Radford, R. Wyles, J. Wyles, J. Varesi, M. Ray, D. Murphy, A. Kennedy, A. Finch, E. Moody, F. Cheung, R. Coda, S. Baur, Infrared Technol. Appl. XXIV 3436 (1998) 636.
[20] W. Radford, D. Murphy, A. Finch, K. Hay, A. Kennedy, M. Ray, A. Sayed, J. Wyldes, R. Wyldes, J. Varesi, E. Moody, F. Cheung, Infrared Technol. Appl. XXV SPIE-3698 (1999) 119.
[21] J.F. Belcher, C.M. Hanson, H.R. Beratan, K.R. Udayakumar, K.S. Soch, Infrared Technol. Appl. XXIV 3436 (1998) 611.
[22] J.K. Gimzewski, C. Gerber, E. Meyer, R.R. Schlittler, in: Micromechanical Heat Sensor: Observation of a Chemical Reaction, Photon and Electrical Heat Pulses, 1995, Kluwer Academic Publisher, Dordrecht, 1995, p. 123.
[23] R. Amantea, L.A. Goodman, F. Pantuso, D.J. Sauer, M. Varhese, T.S. Villianni, L.K. White, Infrared Technol. Appl. XXIV 3436 (1998) 647.
[24] P.G. Datskos, S. Rajic, I. Datskou, Appl. Phys. Lett. 73 (1998) 2319.
[25] P.G. Datskos, S. Rajic, I. Datskou, C.M. Egert, IR Detectors Focal Plane Arrays V SPIE-3978 (1998) 173.
[26] P.G. Datskos, S. Rajic, C.M. Egert, I. Datskou, Infrared Technol. Appl. XXV SPIE-3698 (1999) 151.
[27] P.G. Datskos, Photodetector Mater. Dev. V SPIE-3948 (2000) 80.
[28] D. Sarid, Scanning Force Microscopy, Oxford University Press, New York, 1991.
[29] J.H. Hoh, J.P. Cleveland, J.-P. Prater, P.K. Hansma, J. Am. Chem. Soc. 114 (1992) 4917.
[30] P.J. Shaver, Rev. Sci. Instr. 40 (1969) 901.
[31] P.W. Kruse, Microcantilever Infrared Detector, Internal ORNL Report, 1999.
[32] P.G. Datskos, S. Rajic, L.R. Senesac, D.D. Earl, B.M. Evans, J.L. Corbeil, I. Datskou, Infrared Technol. Appl. XXVI SPIE, in press.
[33] T. Thundat, P.I. Oden, P.G. Datskos, G.Y. Chen, R.J. Warmack, in Microcantilever Sensors, Oak Ridge, Tennessee, 1996.
[34] R.M. White, J. Appl. Phys. 34 (1963) 3559.
[35] H.K. Wickramasinghe, R.C. Bray, V. Jipson, C.F. Quate, J.R. Salcedo, Appl. Phys. Lett. 33 (1978) 923.
[36] T. Figielski, Phys. Stat. Sol. 1 (1961) 306.
[37] R.G. Stearns, G.S. Kino, Appl. Phys. Lett. 47 (1985) 1048.
[38] P. Hess, A.C. Boccara, Photoacoustic, Photothermal and Photochemical Processes at Surfaces and in Thin Films, Springer, Berlin, 1989.
[39] P.G. Datskos, S. Rajic, I. Datskou, Ultramicroscopy 82 (2000) 42.
[40] J. Lai, T. Perazzo, Z. Shi, A. Majumdar, Sensors and Actuators 58 (1997) 113.
[41] R.P. Feynman, R.B. Leighton, M. Sands, The Feynman Lectures on Physics, Vol. 2, 13th Edition Addison-Wesley Publishing Company, Reading, MA, 1964.
[42] G.A. West, J.J. Barrett, D.R. Siebert, K.V. Redy, Rev. Sci. Instr. 54 (1983) 797.
[43] P. Aigrain, M. Balkanski, Selected Constants of Semiconductors, Pergamon Press, New York, 1961.
[44] R.J. Young, Vacuum 44 (1993) 353.
[45] M.J. Vasile, C. Biddick, S. Schwalm, J. Vac. Sci. Technol. B12 (1994) 2388.
[46] T. Ishanti, T. Ohnishi, Y. Kawanami, Jap. J. Appl. Phys. 29 (1990) 2283.
[47] G. Meyer, N.M. Amer, Appl. Phys. Lett. 53 (1988) 1045.
[48] R.C. Weast, Handbook of Chemistry and Physics, 59th Edition, CRC, Florida, 1972.